Hot-phonon effect on power dissipation in a biased $Al_xGa_{1-x}N/AlN/GaN$ channel

M. Ramonas,* A. Matulionis, and J. Liberis

Semiconductor Physics Institute, A. Goštauto 11, Vilnius 01108, Lithuania

L. Eastman, X. Chen, and Y.-J. Sun

Cornell University, 425 Phillips Hall, Ithaca, New York 14853, USA

(Received 23 August 2004; revised manuscript received 29 October 2004; published 25 February 2005)

The Monte Carlo simulation of hot-electron energy dissipation is carried out for a biased AlGaN/AlN/GaN channel. The conduction band profile and electron wave functions are calculated through self-consistent solution of Poisson and Schrödinger equations. Nonelastic scattering of electrons on acoustic phonons and nonequilibrium longitudinal optical (LO) phonons is included. The nonequilibrium LO phonons are treated in terms of hot-phonon lifetime. The dependence of electron temperature and dissipated power on the applied electric field is obtained from the Monte Carlo simulation. The experimental results on noise temperature and current as functions of electric field strength applied along the channel are presented, and the dependence of the supplied electric power on the inverse electron temperature is evaluated. The best agreement between the Monte Carlo results and the experimental data is obtained for the hot-phonon lifetime $\tau_{ph}=1$ ps.

I. INTRODUCTION

Gallium nitride and related compounds have become of increasing interest for use in many semiconductor devices.[1] A wide band gap of GaN, together with high thermal conductivity bodes well for device high-power operation. Despite the wide band gap and large electron effective mass, the measured electron drift velocity reaches values[2] suitable for device high-speed performance. A high-density two-dimensional electron gas (2DEG) in the nitride heterostructure channels can be obtained without intentional doping.[3]

An AlGaN/GaN high electron mobility transistor (HEMT) is an excellent device for generation of microwave power at 10 GHz microwave frequency,[4] for recent data see Refs. 5. The cutoff frequency of well-designed AlGaN/GaN HEMTs is determined by electron drift velocity in the 2DEG channel: $\sim 1.15 \times 10^7$ cm/s is extracted from the dependence of the cutoff frequency on reciprocal gate length.[6] The estimated drift velocity value for these HEMTs is lower than expected from Monte Carlo simulation.[7] Moreover, the measured electron drift velocity peaks at 7×10^7 cm/s in a biased GaN *p-i-n* diode illuminated with a femtosecond optical pulse.[2] This value exceeds considerably the drift velocity in the 2DEG channel. Of course, the conditions differ in *p-i-n* diodes and HEMTs, and a detailed investigation of electron energy dissipation in nitride 2DEG channels is needed for a better understanding of electron transport at high electric fields.

Several sources of such discrepancy can be pointed out. The microwave noise measurements indicate that the GaN layer shares the high-energy electrons with the AlGaN layer.[8] The electron penetration into AlGaN is known to degrade high-frequency performance of nitride channels for HEMT's. AlN can be used as a barrier material to inhibit the electron penetration. However, lattice mismatch of AlN and GaN makes it difficult to grow perfect heterostructures with thick AlN barrier layers. On the other hand, a thin pseudomorphic layer of AlN can be successfully inserted between the AlGaN and GaN layers.[9]

Under conditions of a high electric field and a small volume, the supplied electric power density is extremely high, and channel self-heating takes place. The Joule heat is known to reduce electron saturation velocity and transistor performance. Short voltage pulses have been used for experimental investigation, and the self-heating effect on drift velocity was avoided.[10,11]

Emission of longitudinal optical (LO) phonons is the main energy dissipation mechanism for high-energy electrons in nitride channels. Because of low group velocity, the emitted LO phonons stay in the channel until they either are reabsorbed by electrons or decay into acoustic or other phonon modes; the latter transfer the excess energy to a heat sink. In nitride materials, the LO-phonon decay time, termed lifetime, exceeds considerably the time of LO-phonon emission by a hot electron. As a result, accumulation of nonequilibrium LO phonons, termed hot phonons, takes place.[12–14] In particular, hot-phonon reabsorption slows down the electron energy dissipation. An almost immediate emission of the reabsorbed phonon causes randomization of electron motion and, hence, the electron drift velocity decreases.

In this paper, hot-phonon effects are studied experimentally and through Monte Carlo simulation for AlGaN/AlN/GaN and AlGaN/GaN heterostructures. Hot-electron noise temperature and current are measured under conditions when the effects of electron sharing and lattice Joule heating are avoided, the hot-electron temperature and the dissipated power per electron are estimated from the Monte Carlo calculations.

II. CONDUCTION BAND PROFILE AND ELECTRON WAVE FUNCTIONS

The Monte Carlo calculations are carried out for wurtzite, Ga-face AlGaN/AlN/GaN channel. The wurtzite group III nitrides GaN and AlN, are tetrahedrally coordinated semiconductors; a hexagonal Bravais lattice contains four atoms

per unit cell. For binary compounds with wurtzite structure, the sequence of the atomic layers of the two constituents is reversed along the c axis. In the case of GaN, a basal surface is either Ga or N faced. The modeled structure is chosen to be Ga face with the c axis taken to be perpendicular to the AlN/GaN interface. The heterostructure consists of a 12 nm $Al_{0.33}Ga_{0.67}N$ layer, 1.5 nm AlN layer, and a thick GaN layer.

Heterostructure is intentionally undoped. In nitride structures, a high density 2DEG forms without doping due to polarization difference in the layers. Spontaneous polarization of AlN, GaN, and AlGaN exists at zero strain. It is often assumed that the positive direction of a polarization goes from a gallium atom (cation) to the nearest nitrogen (anion) atom.

The spontaneous polarization P_{SP} is negative and its value differs in AlN, GaN, and AlGaN:[3]

$$P_{SP}(Al_xGa_{1-x}N) = (-0.052x - 0.029)C/m^2. \qquad (1)$$

Under strain, piezoelectric polarization is induced in addition to the spontaneous polarization. The piezoelectric polarization is negative for tensile and positive for compressive strained layers, respectively. In the heterostructure under consideration, the thin AlGaN and AlN layers grown onto the thick GaN buffer layer are under tensile strain. The piezoelectric polarization in the AlGaN alloy layer grown on the GaN, in the direction of the c axis, can be determined by[3]

$$P_{PE}(Al_xGa_{1-x}N) = 2\frac{a(0) - a(x)}{a(x)}\left(e_{31}(x) - e_{33}(x)\frac{C_{13}(x)}{C_{33}(x)}\right), \qquad (2)$$

where $a(0)$ and $a(x)$ are the lattice constants in GaN and AlGaN, respectively, P_{PE} is the piezoelectric polarization, e_{ij} are the piezoelectric coefficients, C_{ij} are the elastic constants. The piezoelectric and spontaneous polarizations point in the same direction; this increases the difference in the values of the overall polarization of the heterostructure layers. The spatial gradient of the polarization at an abrupt interface between the top and the bottom layers induces fixed charge density given by

$$\sigma = [P_{PE}(\text{bottom}) + P_{SP}(\text{bottom})] - [P_{PE}(\text{top}) + P_{SP}(\text{top})]. \qquad (3)$$

For AlGaN/AlN/GaN heterostructure, the charge density σ/e (e is the electron charge) is negative at the AlGaN/AlN/ interface (-4.5×10^{13} cm^{-2}), and the charge density is positive between AlN and GaN layers (6.4×10^{13} cm^{-2}). The resultant fixed polarization-induced charge is positive, and free electrons tend to compensate it. This causes formation of the 2DEG in the GaN layer near the interface. The 2DEG density is assumed to be 1.4×10^{13} cm^{-2} for the modeled AlGaN/AlN/GaN heterostructure. Additional negative charge is introduced on the AlGaN surface to account for the surface states occupied by electrons. The negative residual acceptor charge is introduced in the GaN buffer for a better 2DEG confinement.

Poisson equation should be solved to obtain the conduction band profile for the known charge distribution. In heterostructures with a low 2DEG density, the charge of free
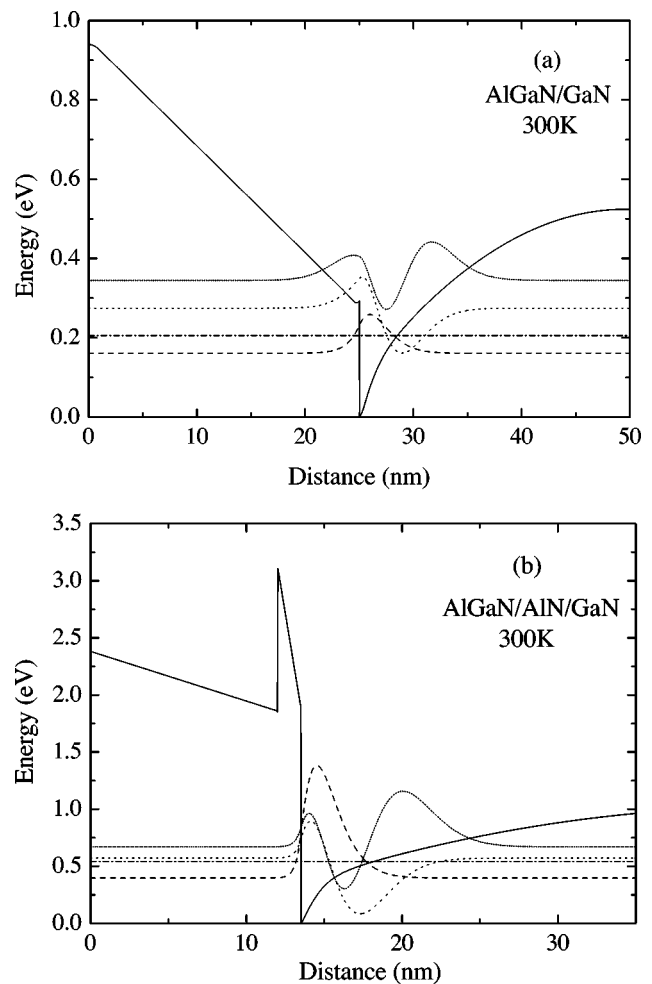

FIG. 1. The potential profile (solid line) and the first three confined-electron wave functions, for AlGaN/GaN (a) (Ref. 13) and AlGaN/AlN/GaN (b) heterostructures. The dashed, dotted, and short-dotted lines indicate the envelope functions of the first, second, and third subbands, respectively. The envelope functions are plotted in arbitrary units, and the zero of each wave function is the corresponding eigenenergy. The dash-dotted line is the Fermi energy.

electrons can be ignored and the confining potential can be approximated by a simple triangular function. However, for a high-density 2DEG, this approximation is rather poor and the Schrödinger equation should be solved self-consistently together with the Poisson equation.[15,16] The electron envelope functions and the energy spectra obtained from the Schrödinger equation are used to calculate the free-electron spatial distribution. This distribution, together with the fixed charge distribution, is used to obtain a new potential profile from the Poisson equation. Both the Schrödinger and the Poisson equations are solved consecutively until convergence is reached.

The potential profile and the first three envelope functions at zero electric field and 300 K temperature are shown in Fig. 1. For AlGaN/GaN heterostructure, due to the low interface barrier between AlGaN and GaN, the envelope functions belonging to the second and higher subbands penetrate into AlGaN considerably: the higher-subband electrons are

shared by AlGaN and GaN layers [Fig. 1(a)].[13] The effective mass of a two-dimensional electron moving in parallel to the quantum well plane will be composed of the electron effective mass in the AlGaN barrier and the electron effective mass in the GaN proportionally to the probabilities of finding an electron in the well and in the barrier. So, the electron penetration into the barrier material will change the effective mass and the scattering rates.

The electron penetration into the barrier material is avoided when a thin AlN layer is inserted between AlGaN barrier and GaN channel. The high AlN/GaN interface barrier confines the electrons in the GaN layer [Fig. 1(b)] and induces a high-density 2DEG. Because of the lattice mismatch, only a thin strained (pseudomorphic) layer of AlN can be grown on a thick GaN layer without strain relaxation and cracking.

III. MONTE CARLO MODEL

The scattering probabilities for the Monte Carlo simulation are numerically calculated for the equilibrium self-consistent electron wave functions. In order to save computer time, no field-induced modulation of the subband energies and envelope wave functions is taken into account.

For wurtzite-phase GaN, the conduction band minimum is located at the Γ point (Γ_1). The lowest satellite valleys of the conduction band are at the U point that is two thirds on the way between the L- and M-symmetry points. The higher conduction band valleys are located at the Γ point (Γ_3), at the M point, and at the K point. In the range of electric fields under investigation, electron scattering into the upper valleys is expected to be negligible, and a one-valley (Γ_1) many-subband spherical parabolic model is employed. Electron sharing and real space effects are neglected in our calculations.

Scattering mechanisms included in the simulation are acoustic phonon scattering and LO phonon scattering. Scattering by ionized impurities is not included since the structure under consideration is undoped (the 2DEG is induced by the spontaneous and piezoelectric polarization charges). Our Monte Carlo model neglects interelectron collisions.

Electron scattering by acoustic phonons at room temperature is often treated as an elastic process because the energies of the involved acoustic phonons are small. However, this approximation would mean that electrons could not dissipate energy unless they were accelerated to the energies greater than LO phonon energy. For GaN, the LO phonon energy is quite large, and the low-field results based on the elastic approximation may lead to an inaccurate evaluation of the electron energy dissipation. In our simulation, the electron scattering by acoustic phonons is treated as an inelastic process. We adopt the approximation $q_z \ll q_\parallel$, where $q_\parallel$ is the in-plane component of the acoustic phonon wave vector q, and q_z is the transverse one.[17]

The electrons interact with acoustic phonons through deformation potential and electrostatic polarization associated with atom vibrations. The nitrides exhibit strong piezoelectric effects, and the piezoelectric scattering is comparable to the deformation potential scattering at 300 K.

In wurtzite structures, the deformation potential in the central valley is a diagonal second rank tensor. The value of D_{zz} is generally expected to be different from $D_{xx}=D_{yy}$. To our knowledge, there is no experimentally obtained value of these parameters for GaN available to date. We assume equal diagonal elements and treat the deformation potential tensor as a scalar quantity.[18]

Electron transition probability per unit time from the state $(\mathbf{k}, i)$ to the state $(\mathbf{k}', f)$ for acoustic deformation potential scattering is

$$W_{i \to f}(\mathbf{k}, \mathbf{k}') = \frac{\pi D^2 q_\parallel}{\varrho V v_1} M_{i \to f}(q_z) \left\{ N_{ac}(q_\parallel) + \frac{1}{2} \pm \frac{1}{2} \right\}$$
$$\times \delta[\varepsilon_f(\mathbf{k}') - \varepsilon_i(\mathbf{k}) \pm \hbar v_1 q_\parallel], \qquad (4)$$

where the upper and the lower symbols refer to emission and absorption, respectively, i and f are the indexes of the initial and final subbands, ϱ is the density of the crystal, V is the volume of the crystal, v_1 is the longitudinal sound velocity, D is the deformation potential, $\varepsilon_i(\mathbf{k})$ is the electron energy, and $2\pi\hbar$ is the Planck constant. The overlap integrals $M_{i \to f}(q_z)$ are calculated using self-consistent electron wave functions $\psi_i(z)$:

$$M_{i \to f}(q_z) = \left| \int \psi_i(z) e^{j q_z z} \psi_f(z) dz \right|^2. \qquad (5)$$

$N_{ac}(q_\parallel)$ stands for the average acoustic phonon number, in equilibrium:

$$N_{ac}(q_\parallel) = \frac{1}{\exp\left(\dfrac{\hbar v_1 q_\parallel}{k_B T}\right) - 1}. \qquad (6)$$

The strength of the electron scattering with acoustic phonons via piezoelectric interaction is determined by the dimensionless electromechanical coupling coefficient. This quantity contains contributions both for longitudinal (LA) and transverse acoustical (TA) phonons. In our calculations we perform angular averaging and obtain for the electromechanical coupling coefficient[19]

$$K^2 = \frac{e_{LA}^{*2}}{\varepsilon_0 \varepsilon_s c_{LA}} + \frac{e_{TA}^{*2}}{\varepsilon_0 \varepsilon_s c_{TA}}, \qquad (7)$$

where c_{LA}, c_{TA}, e_{LA}^*, and e_{TA}^* are the angular averages of the elastic and piezoelectric constants, ε_0 is the permittivity of free space, and ε_s is the static dielectric constant. The electron transition rate for acoustic piezoelectric interaction is

$$W_{i \to f}(\mathbf{k}, \mathbf{k}') = \frac{\pi e^2 K^2 v_1}{\varepsilon_0 \varepsilon_s V q_\parallel} \frac{q_\parallel^2}{(q_\parallel + q_0)^2} M_{i \to f}(q_z)$$
$$\times \left\{ N_{ac}(q_\parallel) + \frac{1}{2} \pm \frac{1}{2} \right\}$$
$$\times \delta[\varepsilon_f(\mathbf{k}') - \varepsilon_i(\mathbf{k}) \pm \hbar v_1 q_\parallel], \qquad (8)$$

where q_0 is the inverse screening length.

Electron-optical-phonon coupling in wurtzite crystals is different from the well-known cubic case. The electrons interact both with LO-like and TO-like modes, rather than with

a single LO mode as in the cubic case. But recently it has been shown that the TO-like scattering rate is more than two orders of magnitude lower than the LO-like scattering rate. Moreover, the LO scattering rate in the cubic approximation is valid regardless of the chosen point in the Brillouin zone.[20] In the present, we use the cubic approximation and the formulation of Price for the scattering probabilities, and thus we also assume that the phonons are three dimensional.[21] The electron transition rate for polar optical interaction is

$$
\begin{aligned}
W_{i \to f}(\mathbf{k}, \mathbf{k}') = {}& \frac{\pi e^2}{\varepsilon_0 \varepsilon_\infty V} \frac{(\omega_{LO}^2 - \omega_{TO}^2)}{\omega_{LO} q^2} \frac{q_\parallel^2}{(q_\parallel + q_0)^2} M_{i \to f}(q_z) \\
& \times \left\{ N_{opt}(\mathbf{q}) + \frac{1}{2} \pm \frac{1}{2} \right\} \delta[\varepsilon_f(\mathbf{k}') \\
& - \varepsilon_i(\mathbf{k}) \pm \hbar \omega_{LO}],
\end{aligned}
\tag{9}
$$

where ϵ_∞ is the high-frequency dielectric constant, ω_{LO} is the LO phonon frequency, ω_{TO} is the TO phonon frequency, and $N_{opt}(q)$ is the optical phonon occupation number.

Electron screening is taken into account for the polar optical phonon scattering and the piezoelectric scattering. We have assumed long-wavelength diagonal screening derived from the matrix-random phase approximation[22]

$$
q_0 = \frac{m e^2}{2 \pi \varepsilon_0 \varepsilon_s \hbar^2} \sum_i f_i(0),
\tag{10}
$$

where i is the subband index and $f_i(0)$ is the electron distribution function at the bottom of each subband.

Integration of Eqs. (4), (8), and (9) over all possible final states $\mathbf{k}'$ yields the integrated probability for the electron in the subband i with wavevector $\mathbf{k}$ to be scattered into subband f per unit time. The integration is performed numerically, and the total scattering rates are tabulated for use in the Monte Carlo algorithm.

The uniform electric field is applied along the 2DEG channel, and the electron motion and scattering are treated in a semiclassical way in the framework of ensemble Monte Carlo method.[23] The motion and scattering of 10^6 electrons is simulated for 50 ps time. Figure 2 shows the time dependence of electron drift velocity and LO-phonon population for the initial 5 ps. When we are interested in the steady-state behavior, the transient data are excluded from the averaging.

All constants required in the calculations are the same as in Ref. 13. A high density of 2DEG forces to include degeneracy and hot-phonon effects into our Monte Carlo algorithm. The rejection technique proposed by Lugli and Ferry[24] is used to treat the degeneracy.

IV. HOT PHONONS

The ensemble Monte Carlo technique can be used to follow the time evolution of LO-phonon distribution function and evaluate phonon induced modifications to the electron transport in the semiconductor heterostructures.[11,25,26] The time-dependent LO-phonon distribution $N_{opt}(\mathbf{q})$ is calculated by setting up a histogram $h_{ph}(t)$ defined over the grid in the phonon wave vector space $\mathbf{q}$. As the external electrical field
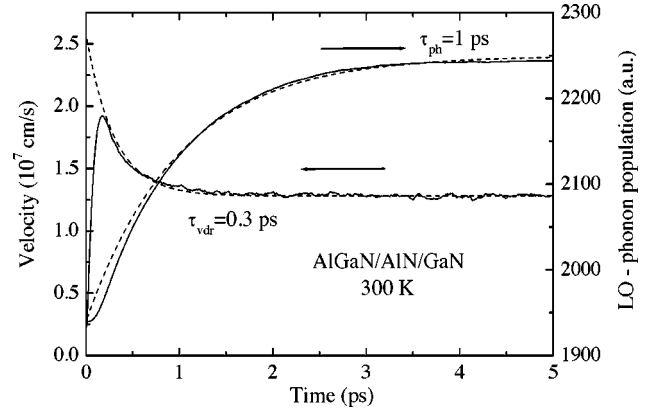

FIG. 2. The time dependence of electron drift velocity (solid line, left axis) and LO-phonon population (solid line, right axis) for the initial 5 ps of the electron motion in 30 kV/cm field. The dashed lines are the exponential function approximations with $\tau_{ph} = 1$ ps and $\tau_{VDR} = 0.3$ ps.

breaks the symmetry, it is not enough to follow the distribution of the **q** amplitude, and full phonon distribution function should be considered.

At the beginning of the simulation, the mesh $N_{opt}(t=0)$ and the histogram $h_{ph}(t=0)$ are set to the equilibrium value given by Bose distribution function. Under the reasonable assumption of dispersionless LO phonons, $N_{opt}(t=0)$ is independent on phonon wave vector. During the simulation, after each LO phonon emission (absorption) event, Δh_{ph} is added to (subtracted from) the corresponding cell of the histogram h_{ph}; the actual electron density n_e and the number of simulated particles N_{sim} is taken into account as follows:

$$
\Delta h_{ph} = \left(\frac{2\pi}{\Delta q_x} \right) \left(\frac{2\pi}{\Delta q_y} \right) \left(\frac{2\pi}{\Delta q_z} \right) \left(\frac{n_e}{N_{sim} L_{eff}} \right),
\tag{11}
$$

where $\Delta q_x \times \Delta q_y \times \Delta q_z$ is the volume of the cell in the **q** space and L_{eff} is the effective channel width. Due to low group velocity of the LO phonons, the launched phonons are assumed to remain in the 2DEG channel.

The excess LO phonons decay via anharmonic interaction into the zone-boundary phonons which weakly interact with electrons. Those phonons, in turn, rapidly decay into acoustic modes of the thermal bath. This complex phonon process, acts as an efficient sink of energy and momentum for the electron-LO-phonon subsystem. To account for the nonequilibrium LO-phonon decay we use relaxation-time approximation. At fixed times $i\Delta T$, $i=1,\ldots,M$ during the simulation (with ΔT shorter than the average LO-phonon scattering time), h_{ph} is updated through

$$
h'_{ph}(i\Delta T) = h_{ph}(i\Delta T) - [h_{ph}(i\Delta T) - h_{ph}(0)] \frac{\Delta T}{\tau_{ph}},
\tag{12}
$$

where τ_{ph} is the LO-phonon relaxation time (the lifetime with respect to their decay into other phonons). The LO-phonon lifetime can be determined experimentally or used as a fitting parameter in the Monte Carlo simulation. The best agreement between our Monte Carlo calculations and experimental results is obtained for $\tau_{ph} = 1$ ps.
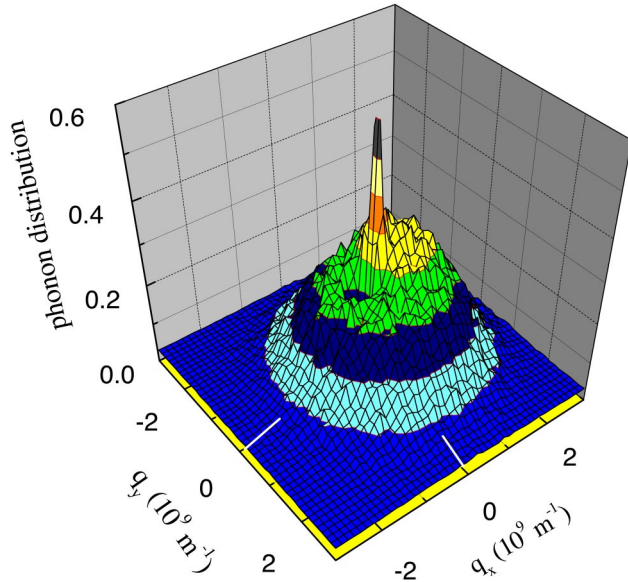
FIG. 3. The LO-phonon distribution function for AlGaN/AlN/GaN heterostructure at room temperature and 20 kV/cm electric field (applied in the x direction).

$N_{opt}(t)$ is refreshed at the end of each time step using the histogram h_{ph}. The rejection technique is used to avoid electron-LO-phonon scattering rate recalculation at the end of the each time step. The convenient maximum value N_{max} (the maximum of the phonon distribution) is chosen in place of the actual **q**-dependent LO-phonon distribution function in the electron-LO-phonon scattering rates (9), and overall scattering rates are calculated at the beginning of the simulation. The artificial increase in electron scattering rates due to N_{max} is compensated through rejection technique. Once the final electron state after scattering is known, the wave vector of the LO phonon involved in the scattering event can be determined. The evenly distributed between 0 and N_{max} random number r is generated and compared with the phonon occupation number N_c of the cell associated with wave vector of the phonon involved in the scattering. If $r < N_c$ the transition is accepted, and else the scattering event is treated as a self-scattering one. The computer time for taking care of self-scattering events is more than compensated for by the simplification of the procedure.

The cross section (for transverse phonon component $q_z = 0$) of simulated LO-phonon distribution function for AlGaN/AlN/GaN heterostructure at room temperature and 20 kV/cm electric field is displayed (Fig. 3). The LO-phonon occupancy exceeds the equilibrium one in the limited **q**-plane area. Due to energy and momentum conservation the electrons cannot emit phonons with wave vector values close to zero. The distribution of hot phonons is shifted in the direction of the applied electric field. Strong electron-LO-phonon interaction supports a streaming motion of some electrons in nitride heterostructure. When a lucky accelerated electron reaches energy $\varepsilon = \hbar\omega_{LO}$ without being scattered, it shortly emits LO phonon, returns to the state near $\varepsilon \approx 0$ and repeats the acceleration and emission many times. The emitted LO phonons are almost identical, they form a sharp peak at the corresponding **q** value. The peak
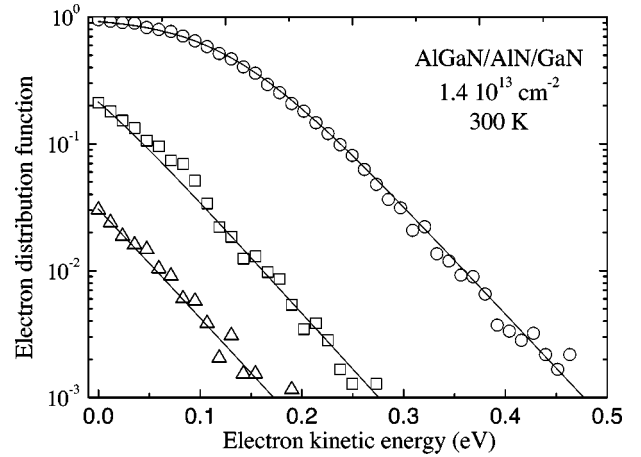

FIG. 4. The simulated hot-electron distribution functions for AlGaN/AlN/GaN heterostructure at 300 K lattice temperature and 10 kV/cm applied electric field. Circles, squares, and triangles stand for the first, second, and third subband, respectively. The solid lines are fitted Fermi-Dirac distribution functions. Estimated electron temperature is $T_e = 590$ K.

is clearly resolved over the washed-out hot-phonon distribution (Fig. 3).

V. ELECTRON TEMPERATURE AND NOISE TEMPERATURE

The simulated electron distribution functions for the first three subbands of the AlGaN/AlN/GaN heterostructure are presented in Fig. 4 (symbols). The 2DEG in the first subband is degenerate: low-energy electron occupation number is close to 1. The simulated functions are fitted with Fermi-Dirac distribution function (Fig. 4, solid lines); the same electron temperature and Fermi energy are used for each subband.

A reasonably good fitting is obtained for the field range $E < 35$ kV/cm. At a higher field, the electron distribution function acquires a high energy tail that can be attributed to electron runaway. The electron temperature is not applicable to the runaway electrons, but the fitting survives for the majority of the electrons present in the energy range below 0.5 eV (the tail electrons make approximately 20% of all electrons at 50 kV/cm).

In experiment, the electron temperature is estimated from the microwave noise measured for two-terminal samples supplied with coplanar ohmic electrodes and subjected to electric field applied in the 2DEG plane. The channel length and the electrode width were, respectively, $L = 7$ μm and $w = 120$ μm for AlGaN/GaN and $L = 5$ μm and $w = 100$ μm for AlGaN/AlN/GaN. The low-field Hall mobility is $\mu_0 = 1100$ cm^2/(V s) for AlGaN/GaN and $\mu_0 = 1152$ cm^2/(V s) for AlGaN/AlN/GaN heterostructures. The layer structure of the experimentally investigated AlGaN/GaN and AlGaN/AlN/GaN heterostructures are described in Sec. II (Fig. 1). The current-field characteristics are measured using two different voltage pulse durations 0.15 and 2 μs (Fig. 5). The lattice self-heating effect be-
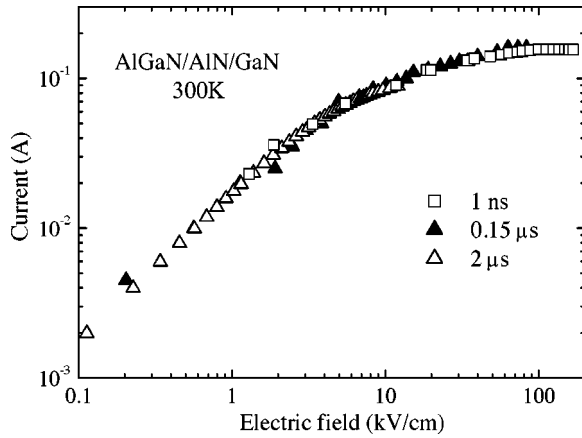
FIG. 5. The current dependence on applied electric field for AlGaN/AlN/GaN heterostructure at 300 K lattice temperature. The voltage-pulse duration: 1 ns (open squares) (Ref. 27), 0.15 μs (closed triangles), 2 μs (open triangles). The estimated saturation velocity is 1.1×10^7 cm/s.

comes pronounced at 10 kV/cm field when the voltage pulse is 2 μs, and at 100 kV/cm for 0.15 μs pulses.

The hot-electron longitudinal noise was investigated at a 10 GHz microwave frequency, where generation-recombination, flicker, and other noise sources can be neglected. The noise temperature is measured with a gated radiometer when the pulsed voltage is applied: 0.15 μs pulses are used at high electric fields, and 2 μs pulses are used at low and moderate electric fields (the technique is described in Ref. 28). Figure 6 presents the noise temperature as a function of the applied electric field for both heterostructures under investigation. The main sources of noise are caused by kinetic motion of the electrons, by electron-temperature fluctuations, and by electron sharing. For a detailed analysis of hot-electron noise in AlGaN/GaN see, for example, Ref. 29.

At electric fields up to 7 kV/cm, the noise temperature is nearly the same for AlGaN/GaN and AlGaN/AlN/GaN heterostructures. The electrons are confined in the GaN channel
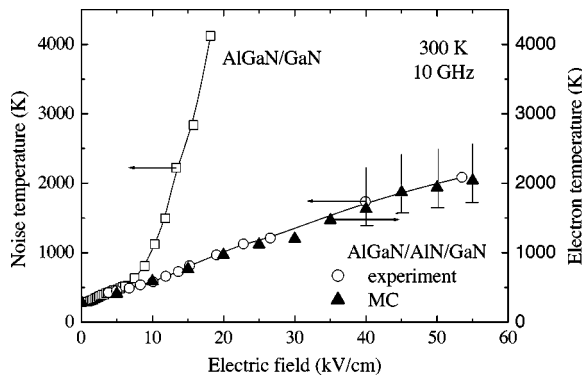

FIG. 6. The field-dependent hot-electron longitudinal noise temperature at 10 GHz frequency at 300 K temperature for AlGaN/GaN (open squares, left axis) and AlGaN/AlN/GaN (open circles, left axis) heterostructures. The solid lines guide the eye. The closed triangles (right axis) represent the electron temperatures evaluated from the Monte Carlo results. The vertical bars indicate errors.
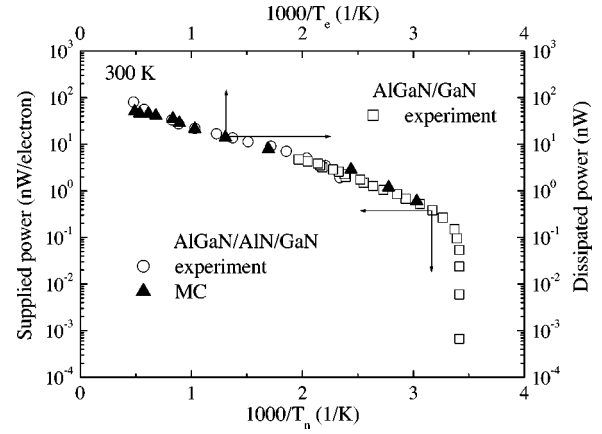

FIG. 7. The supplied electric power per electron against inverse noise temperature (experimental results, down and left axes). The open circles—AlGaN/AlN/GaN heterostructure, the open squares—AlGaN/GaN heterostructure. The Monte Carlo results (close triangles, up and right axes) stand for the dissipated power as a function of inverse electron temperature for the AlGaN/AlN/GaN heterostructure.

in both heterostructures. At a higher electric field, the difference appears: the electron sharing starts, and the additional noise source due to electron sharing emerges in the AlGaN/GaN heterostructure (Fig. 6, open squares). The AlN barrier prevents electron penetration into AlGaN barrier, and the noise due to electron sharing effect is absent at electric fields under investigation (Fig. 6, open circles). The estimation shows that the performed noise temperature measurements provide with the electron temperature data with a better than 20% accuracy in the field range where the sharing is not important.

Figure 6 compares the experimental results on the longitudinal noise temperature (open circles) with the electron temperature obtained through fitting the Monte Carlo results with the Fermi-Dirac distribution (closed triangles). A good agreement between the simulation results and the experimental ones is obtained. This confirms that the electron sharing noise and the noise due to electron-temperature fluctuations are negligible in the AlGaN/AlN/GaN heterostructure in the electric fields up to 55 kV/cm, and the electron temperature can be evaluated from the experimental results on longitudinal noise temperature.

VI. POWER DISSIPATION

The experimental results on current and noise temperature provide with the dependence of electron temperature on supplied electric power. The supplied electric power per electron P_s is

$$P_s = e v_d E, \tag{13}$$

where v_d is the electron drift velocity and E is the electric field strength applied along the channel.

Figure 7 presents the experimental results on supplied electric power per electron as a function of the inverse noise temperature. Open squares stand for the AlGaN/GaN hetero-
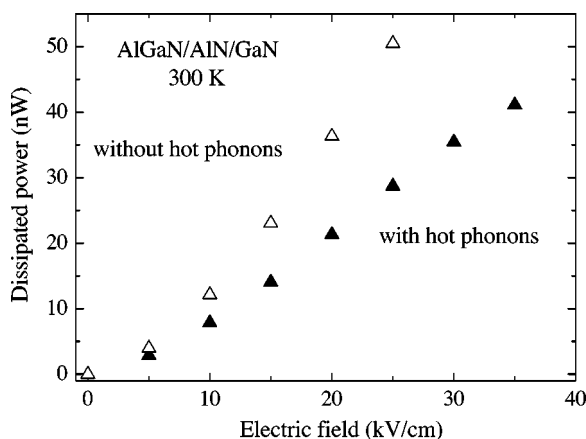
FIG. 8. The dependence of dissipated power on applied electric field for AlGaN/AlN/GaN obtained through Monte Carlo simulation. Open triangles: without hot-phonon effect, closed triangles: with hot-phonon effect.

structure in the range, where the electron temperature can be evaluated from the measured noise temperature. Open circles present data for the AlGaN/AlN/GaN heterostructure.

Under the steady state conditions, the power received from the applied electric field equals the power dissipated by the electrons. The dissipated power is directly evaluated during the Monte Carlo simulation. After each electron scattering event, the change of electron energy during the scattering event is recorded. The total energy change is normalized to the simulated electron number and the simulated electron flight time. The results for AlGaN/AlN/GaN are shown as closed triangles in the Fig. 7. The experimental results on the supplied power are in a good agreement with the Monte Carlo results on dissipated power. This indicates that all scattering mechanisms responsible for the power dissipation are included into the Monte Carlo model. The only fitting parameter in the Monte Carlo algorithm is the hot LO phonon decay time. The best agreement is obtained for the hot-phonon lifetime $\tau_{ph}=1$ ps.

Figure 8 presents the Monte Carlo results on the dissipated power against the applied electric field. In the field range where the energy dissipation is controlled by the LO phonons, the hot phonon effect is evident. The open triangles stand for the results without the hot-phonon effect and full triangles take into account the hot phonons (the decay time $\tau_{ph}=1$ ps). The enhanced phonon occupancy in the limited part of the LO phonon space **q** supports stronger electron-LO-phonon interaction due to stimulated emission and reabsorption of the nonequilibrium LO phonons. On the other hand, the hot-phonon reabsorption slows down the energy dissipation (Fig. 8 open and closed triangles).

VII. DISCUSSION

When the hot-phonon effect is not included into Monte Carlo procedure, the electron energy distribution has a kink near the optical phonon energy.[12] The electrons with energy, higher than the LO-phonon energy, quickly emit LO phonons and are transferred to the low-energy region. Due to this kink the electron-temperature approximation fails.

Hot phonons influence the electron distribution. In particular, the kink at the optical phonon energy disappears, the electron mean energy increases.[12,14] Thus, the electron temperature can be introduced in the field range up to 35 kV/cm (Fig. 6) when the hot phonons are taken into account even if electron-electron scattering is ignored.

At high electric fields ($E > 35$ kV/cm), the high-energy tail develops in the electron distribution function. This behavior can be attributed to the electron runaway. The runaway electrons cannot be described by the effective electron temperature, and the temperature of the electron subsystem is evaluated only approximately (Fig. 6, vertical bars).

The overshoot of the electron drift velocity transient is due to hot-phonon effect (Fig. 2, left axis, solid line). Indeed, it takes time for the hot-phonon population to build up and reach the steady state. During this time, the electron-LO-phonon scattering rate gradually increases. As a result, the drift velocity passes the maximum value and decreases down to its steady-state value. The electron drift velocity and LO-phonon population transients can be approximated by exponential functions (Fig. 2, dashed lines). The electron drift velocity reaches the stationary value faster ($\tau_{VDR}=0.3$ ps) than LO-phonon population ($\tau_{ph}=1$ ps). In the linear situation, the relaxation times should coincide. However, the electron transport is described by the system of nonlinear equations when the electron gas degeneracy and hot-phonon effects are included. As a result, the electron drift velocity can relax faster than the LO-phonon population.

VIII. CONCLUSIONS

The experimental investigation of microwave noise shows that the 1.5 nm AlN interbarrier is efficient in preventing the hot-electron penetration from GaN channel into the adjacent AlGaN barrier. The hot-phonon effects are essential in the investigated AlGaN/AlN/GaN heterostructure: the hot phonons slow down the hot-electron power dissipation and reduce the steady-state drift velocity. When the hot phonons are included into Monte Carlo algorithm a reasonable agreement with the experimental data on the noise temperature and the dissipated power is obtained.

*Electronic address: ramonas@pfi.lt

[1] H. Morkoç, *Nitride Semiconductors and Devices* (Springer, Berlin, 1999).

[2] M. Wraback, H. Shen, J. C. Carrano, C. J. Collins, J. C. Campbell, R. D. Dupuis, M. J. Schuman, and I. T. Ferguson, Appl. Phys. Lett. **79**, 1303 (2001).

[3] O. Ambacher, B. Foutz, J. Smart, J. R. Shealy, N. G. Weimann, K. Chu, M. Murphy, A. J. Sierakowski, W. J. Schaff, L. F. Eastman, R. Dimitrov, A. Mitchell, and M. Stutzmann, J. Appl. Phys. **87**, 334 (2000).

[4] L. F. Eastman, V. Tilak, V. Kaper, J. Smart, R. Thompson, B. Green, J. R. Shealy, and T. Prunty, Phys. Status Solidi A **194**, 433 (2002).

[5] U. K. Mishra, in 62nd Device Research Conference Digest (IEEE Cat. No. 04TH8724) 2004, p.3.

[6] A. Vertiatchikh, W. J. Schaff, and L. F. Eastman, in 2003 International Symposium on Compound Semiconductors (IEEE Cat. No. 03TH8675) 2003, p. 53.

[7] T. -H. Yu and K. Brennan, J. Appl. Phys. **91**, 3730 (2002).

[8] A. Matulionis, J. Liberis, I. Matulionienė, M. Ramonas, L. F. Eastman, J. R. Shealy, V. Tilak, and A. Vertiatchikh, Phys. Rev. B **68**, 035338 (2003).

[9] I. P. Smorchkova, L. Chen, T. Mates, D. Jena, L. Shen, S. Heikman, B. Moran, S. Keller, S. P. DenBaars, J. S. Speck, and U. K. Mishra, J. Appl. Phys. **90**, 5196 (2001).

[10] L. Ardaravičius, A. Matulionis, J. Liberis, O. Kiprijanovic, M. Ramonas, L. F. Eastman, J. R. Shealy, and A. Vertiatchikh, Appl. Phys. Lett. **83**, 4038 (2003).

[11] J. M. Barker, D. K. Ferry, S. M. Goodnick, D. D. Koleske, A. Allerman, and R. J. Shul, J. Vac. Sci. Technol. B **22**, 2045 (2004).

[12] G. Paulavičius, V. V. Mitin, and N. A. Bannov, J. Appl. Phys. **82**, 5580 (1997).

[13] M. Ramonas, A. Matulionis, and L. Rota, Semicond. Sci. Technol. **18**, 118 (2003).

[14] M. Ramonas and A. Matulionis, Semicond. Sci. Technol. **19**, S424 (2004).

[15] A. M. Cruz Serra and H. Abreu Santos, J. Appl. Phys. **70**, 2734 (1991).

[16] R. M. Chu, Y. G. Zhou, Y. D. Zheng, P. Han, B. Shen, and S. L. Gu, Appl. Phys. Lett. **79**, 2270 (2001).

[17] B. K. Ridley, Rep. Prog. Phys. **54**, 169 (1991).

[18] J. Kolnik, I. H. Oguzman, K. F. Brennan, R. Wang, P. P. Ruden, and Y. Wang, J. Appl. Phys. **78**, 1033 (1995).

[19] B. K. Ridley, B. E. Foutz, and L. F. Eastman, Phys. Rev. B **61**, 16 862 (2000).

[20] C. Bulutay, B. K. Ridley, and N. A. Zakhleniuk, Phys. Rev. B **62**, 15 754 (2000).

[21] P. J. Price Ann. Phys. (N.Y.) **133**, 217 (1981).

[22] S. M. Goodnick and P. Lugli, Phys. Rev. B **38**, 10 135 (1988).

[23] C. Jacoboni and P. Lugli, *The Monte Carlo Method for Semiconductor Device Simulation* (Springer, Vienna, 1989).

[24] P. Lugli and D. K. Ferry, IEEE Trans. Electron Devices **ED-32**, 2431 (1985).

[25] P. Lugli, C. Jacoboni, L. Reggiani, and P. Kocevar, Appl. Phys. Lett. **50**, 1251 (1987).

[26] R. Mickevicius and A. Reklaitis, Solid State Commun. **64**, 1305 (1987).

[27] L. Ardaravičius, M. Ramonas, O. Kiprijanovic, J. Liberis, A. Matulionis, L. F. Eastman, J. R. Shealy, X. Chen, and Y. J. Sun (unpublished).

[28] A. Matulionis, J. Liberis, L. Ardaravičius, M. Ramonas, I. Matulionienė, and J. Smart, Semicond. Sci. Technol. **17**, L9 (2002).

[29] A. Matulionis and J. Liberis, IEE Proc.-G: Circuits, Devices Syst. **151**, 148 (2004).